J. Fluid Mech. (1996), *vol.* 307, *pp.* 43–62

Transition to turbulence in an elliptic vortex

By T. S. LUNDGREN[1] AND N. N. MANSOUR[2]

[1]Department of Aerospace Engineering and Mechanics, University of Minnesota, Minneapolis, MN 55455, USA

[2]NASA-Ames Research Center, Moffett Field, CA 94035, USA

(Received 25 January 1995 and in revised form 13 September 1995)

Stability and transition to turbulence are studied in a simple incompressible two-dimensional bounded swirling flow with a rectangular planform – a vortex in a box. This flow is unstable to three-dimensional disturbances. The instability takes the form of counter-rotating swirls perpendicular to the axis which bend the vortex into a periodic wave. As these swirls grow in amplitude the primary vorticity is compressed into thin vortex layers. These develop secondary instabilities which roll up into vortex tubes. In this way the flow attains a turbulent state which is populated by intense elongated vortex tubes and weaker vortex layers which spiral around them. The flow was computed at two Reynolds numbers by spectral methods with up to 256^3 resolution. At the higher Reynolds number broad three-dimensional shell-averaged energy spectra are found with nearly a decade of Kolmogorov $k^{-5/3}$ law and small-scale isotropy.

1. Introduction

We study the three-dimensional instability of the two-dimensional flow described by the streamfunction

$$\Psi = \frac{A \sin b_1 x \sin b_2 y}{b_1^2 + b_2^2} \tag{1}$$

and the nonlinear growth of perturbations from this flow. Here $b_1 = \pi/L_1$, $b_2 = \pi/L_2$. This is a swirling flow in a box which is bounded by $0 \leqslant x \leqslant L_1$, $0 \leqslant y \leqslant L_2$ and is infinite in the z-direction. This flow is a solution of the Navier–Stokes equation with $A = \exp(-\nu(b_1^2 + b_2^2)t)$ which slowly decays with time. We seek a viscous solution which starts near this one and slips along the impenetrable boundaries with zero shear stress. The vorticity of the basic flow is $\omega_z = A \sin b_1 x \sin b_2 y$ which has maximum value A at the centre of the box and drops to zero at the boundaries. The resulting flow can be thought of as a captive vortex.

We denote by $E = L_1/L_2$ the aspect ratio of the box. What is interesting about this flow is that when $E \neq 1$ it is unstable to three-dimensional disturbances. Periodic disturbances along the z-direction grow with time causing the captive vortex to distort into a wavy configuration. As the instability grows components of vorticity perpendicular to the z-axis squeeze the vorticity into sheet-like structures. Ultimately these sheets develop secondary instabilities and break up into a turbulent mixture of intense vortex tubes. However, when $E = 1$ the flow is completely stable to small perturbations.

The streamline pattern of the basic flow is elliptical in the central part of the box, with aspect ratio the same as that of the box, becoming more rectangular as the

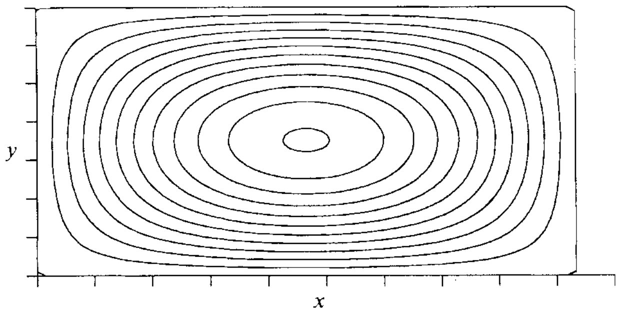

FIGURE 1. Streamline pattern and vorticity contours of the base flow for $E = 2$. Tick marks are at 0.6 intervals in the x-direction and at 0.4 intervals in the y-direction.

boundaries are approached. Figure 1 shows the streamline pattern when $E = 2$. Bayly (1989) has shown, analytically and numerically, that this flow is unstable to high-wavenumber disturbances when the Reynolds number is large. At high wavenumber the instability in this bounded geometry is similar to the broad-band instability in an unbounded flow with elliptical streamlines and uniform vorticity studied by Pierrehumbert (1986), Bayly (1986), Waleffe (1989, 1990) and Landman & Saffman (1987). When the flow is solid body rotation (circular streamlines) stable inertial plane wave perturbation solutions exist in which the wave vector rotates around the axis with an angular velocity which depends on the angle with the axis. At one angle (60°) the velocity field, which is perpendicular to the wave vector, rotates around it in the opposite sense with the same angular velocity and becomes unstable when a plane strain flow is superimposed.

The work which motivated these studies was that of Orszag & Patera (1983). They found, numerically, a three-dimensional instability on a flow which is a superposition of the Blasius boundary layer flow and its primary instability, the Tollmien–Schlichting wave. This flow contains an elongated elliptically shaped swirling region. It is generally believed that this three-dimensional secondary instability plays a major role in transition to turbulence in shear flows (Bayly, Orszag & Herbert 1988).

Earlier work of Gledzer *et al.* (1974, 1975) showed instability in a swirling flow within an elliptic cylinder. The experiment consisted of rotating a water-filled elliptic cylinder until solid body rotation was achieved. Upon stopping the cylinder the water continues to swirl in the container with approximately elliptical streamlines. It was observed that the flow rapidly developed eddies perpendicular to the rotation axis, with one or more cells depending on the length of the the cylinder. Malkus (1989) did clever experiments along these lines with a water-filled flexible cylinder which was made elliptical by rotating it between stationary rollers. In this flow the unstable wave grows for some time and then rapidly flashes into small-scale turbulence. The turbulence decays and when the system spins up again the unstable process repeats.

There is another class of flows which is closely related to the present work. This is the bending instability of a sharp-edged vortex with uniform vorticity exposed to a transverse straining flow treated by Widnall, Bliss & Tsai (1974), Moore & Saffman (1975) and Robinson & Saffman (1984). Wavy disturbances grow on the vortex with wavelength comparable to the dimensions of the vortex. The qualitative explanation is more straightforward than for the homogeneous elliptic flows described above. Moore & Saffman (1975) showed that in the absence of the straining flow stable non-rotating planar waves exist. The strain causes such a wave to align with and grow along the plane of maximum strain rate. In our flow the vorticity distribution rises smoothly to a maximum at the centre instead of being sharp-edged and there are finite boundaries, nevertheless the stability results at low wavenumber are very similar to those of Robinson & Saffman.

In the present work we show numerically that the basic flow described by (1) is unstable at modest axial wavenumbers when the Reynolds number is greater than a critical value. In § 2 we present stability diagrams which superficially resemble those for two-dimensional parallel flows. In § 3 we present the results of nonlinear computations which clearly show transition to turbulent flow by the rollup of vortex sheets into elongated vortex tubes. Homogeneous turbulent flows showing populations of long vortex tubes have been computed by Kerr (1985), She, Jackson & Orszag (1990), Vincent & Meneguzzi (1991, 1994), Jimenez *et al.* (1993) and others.

2. Stability analysis

For the stability problem we set $A = 1$, neglecting the slow decay. Formally, we assume that the decay rate of the mean flow is slow compared to the growth rate of the instability. This is similar to the traditional method of studying the stability of a spatially growing boundary layer by treating it as a locally parallel flow. In the usual way we decompose the velocity field into the basic flow $\boldsymbol{U}$ plus a small perturbation $\boldsymbol{u}'$. The linearized equations for $\boldsymbol{u}'$ are

$$\nabla \cdot \boldsymbol{u}' = 0 \tag{2}$$

$$\frac{\partial \boldsymbol{u}'}{\partial t} + \nabla \cdot (\boldsymbol{U}\boldsymbol{u}' + \boldsymbol{u}'\boldsymbol{U}) = -\nabla p' + \nu \nabla^2 \boldsymbol{u}'. \tag{3}$$

We can separate out an exponential function of z and express the remaining functions of x and y, which do not separate further, as Fourier series. The solution is thus represented in the form

$$u' = \exp \mathrm{i}k_z z \, \frac{1}{b_1} \sum_{m,n=-\infty}^{\infty} \tilde{u}(m,n) \exp \mathrm{i}(mb_1 x + nb_2 y), \tag{4}$$

$$v' = \exp \mathrm{i}k_z z \, \frac{1}{b_2} \sum_{m,n=-\infty}^{\infty} \tilde{v}(m,n) \exp \mathrm{i}(mb_1 x + nb_2 y), \tag{5}$$

$$w' = \exp \mathrm{i}k_z z \sum_{m,n=-\infty}^{\infty} \tilde{w}(m,n) \exp \mathrm{i}(mb_1 x + nb_2 y), \tag{6}$$

with a similarly defined pressure variable. (Note that the time dependence in $\tilde{u}, \tilde{v}$ and $\tilde{w}$ is not explicitly shown.) Upon equating coefficients of $\exp \mathrm{i}(k_z z + mb_1 x + nb_2 y)$ and using the continuity equation to eliminate the pressure, we get the following equations:

$$\frac{\partial \tilde{u}(m,n)}{\partial t} = \frac{b_1 b_2 R_x(m,n)}{b_1^2 + b_2^2} - \nu(m^2 b_1^2 + n^2 b_2^2 + k_z^2)\, \tilde{u}(m,n), \tag{7}$$

$$\frac{\partial \tilde{v}(m,n)}{\partial t} = \frac{b_1 b_2 R_y(m,n)}{b_1^2 + b_2^2} - \nu(m^2 b_1^2 + n^2 b_2^2 + k_z^2)\, \tilde{v}(m,n), \tag{8}$$

where

$$R_x(m,n) = F(m,n) - \frac{mb_1^2(mF + nG + k_zH)}{m^2b_1^2 + n^2b_2^2 + k_z^2}, \tag{9}$$

$$R_y(m,n) = G(m,n) - \frac{nb_2^2(mF + nG + k_zH)}{m^2b_1^2 + n^2b_2^2 + k_z^2}, \tag{10}$$

and

$$\begin{aligned} F(m,n) = &-\frac{m}{2}\,[\tilde{u}(m-1,n-1) + \tilde{u}(m-1,n+1) - \tilde{u}(m+1,n-1) - \tilde{u}(m+1,n+1)] \\ &+\frac{n}{4}\,[\tilde{u}(m-1,n-1) - \tilde{u}(m-1,n+1) + \tilde{u}(m+1,n-1) - \tilde{u}(m+1,n+1)] \\ &-\frac{n}{4}\,[\tilde{v}(m-1,n-1) + \tilde{v}(m-1,n+1) - \tilde{v}(m+1,n-1) - \tilde{v}(m+1,n+1)] \\ &-\frac{k_z}{4}\,[\tilde{w}(m-1,n-1) + \tilde{w}(m-1,n+1) - \tilde{w}(m+1,n-1) - \tilde{w}(m+1,n+1)], \end{aligned} \tag{11}$$

$$\begin{aligned} G(m,n) = &-\frac{m}{4}\,[\tilde{v}(m-1,n-1) + \tilde{v}(m-1,n+1) - \tilde{v}(m+1,n-1) - \tilde{v}(m+1,n+1)] \\ &+\frac{n}{2}\,[\tilde{v}(m-1,n-1) - \tilde{v}(m-1,n+1) + \tilde{v}(m+1,n-1) - \tilde{v}(m+1,n+1)] \\ &+\frac{m}{4}\,[\tilde{u}(m-1,n-1) - \tilde{u}(m-1,n+1) + \tilde{u}(m+1,n-1) - \tilde{u}(m+1,n+1)] \\ &+\frac{k_z}{4}\,[\tilde{w}(m-1,n-1) - \tilde{w}(m-1,n+1) + \tilde{w}(m+1,n-1) - \tilde{w}(m+1,n+1)], \end{aligned} \tag{12}$$

$$\begin{aligned} H(m,n) = &-\frac{m}{4}\,[\tilde{w}(m-1,n-1) + \tilde{w}(m-1,n+1) - \tilde{w}(m+1,n-1) - \tilde{w}(m+1,n+1)] \\ &+\frac{n}{4}\,[\tilde{w}(m-1,n-1) - \tilde{w}(m-1,n+1) + \tilde{w}(m+1,n-1) - \tilde{w}(m+1,n+1)]. \end{aligned} \tag{13}$$

Since $\tilde{w}(m,n)$ is given by the continuity equation,

$$\tilde{w}(m,n) = -\frac{m\tilde{u}(m,n) + n\tilde{v}(m,n)}{k_z}, \tag{14}$$

it can be eliminated from R_x and R_y. With these substitutions (7) and (8) are a system of linear equations for $\tilde{u}(m,n)$ and $\tilde{v}(m,n)$ for $-\infty < m,n < \infty$.

The condition that the bounding box be impenetrable requires that u' be zero for the planes $x = 0$ and L_1 for all y and z, and v' be zero for the planes $y = 0$ and L_2 for all x and z. A consistent set of symmetry conditions which ensure these constraints are the following: for all integer values of m, n,

$$\tilde{u}(-m,n) = -\tilde{u}(m,n), \tag{15}$$

$$\tilde{v}(-m,n) = \tilde{v}(m,n), \tag{16}$$

$$\tilde{w}(-m,n) = \tilde{w}(m,n), \tag{17}$$

$$\tilde{u}(m,-n) = \tilde{u}(m,n), \tag{18}$$

$$\tilde{v}(m,-n) = -\tilde{v}(m,n), \tag{19}$$

$$\tilde{w}(m,-n) = \tilde{w}(m,n). \tag{20}$$

It follows from these that $\tilde{u}(0,n) = \tilde{v}(m,0) = 0$, and that $\tilde{u}(0,0) = \tilde{v}(0,0) = 0$. It can be shown from (7) and (8) that these symmetries persist if they are satisfied by the initial conditions. They mean that (7) and (8) only have to be solved on the first quadrant of the (m,n)-plane, i.e. $m = 0,1,2,\ldots,M$, $n = 0,1,2,\ldots,M$, where M is a large integer where we truncate the system. For instance if we write (7) with $m = 0$ and some n this would require $F(0,n)$, and from (11) we see that we would need $\tilde{u}(-1,n-1)$. From (15) this is equal to $-\tilde{u}(1,n-1)$ which is within the solution set. In general the column $m = -1$ and the row $n = -1$ are shifted into the solution set.

From the structure of the equations one can see that an equation for mode (m,n) is only coupled to four neighbouring modes $(m-1,n-1), (m-1,n+1), (m+1,n-1)$, and $(m+1,n+1)$. These are the nearest four on diagonal lines through (m,n), and these four are each coupled to the nearest four on its diagonals, and so on. This means that the modes can be decomposed into two independent 'checkerboard' subsets: the 'even' modes where $m+n$ is an even integer and the 'odd' modes where $m+n$ is an odd integer. This was pointed out by Bayly (1989).

In the numerical work we have taken $E = 2$ and made the equations dimensionless with a characteristic length l and characteristic time A^{-1} where A is the maximum vorticity in the unperturbed flow. The length scale was chosen so that the dimensionless box sides are $L_1 = 5.6$ and $L_2 = 2.8$. The dimensionless equations are then written with the original notations interpreted as dimensionless quantities. In this scheme the Reynolds number (Al^2/ν) is now written as ν^{-1}. One could of course rescale the box so that one of the sides has unit length and rescale the Reynolds number and wavenumbers accordingly. The reason for our particular choice was determined by the requirements of the nonlinear code which will be described in the next section.

Equations (7) and (8) were solved by a second-order Runge–Kutta method over a range of values of the parameters R_e and k_z, the Reynolds number and axial wavenumber respectively. Even or odd modes were excited by taking initial conditions in which all the mode amplitudes were zero except $\tilde{u}(2,0) = 1$ to generate even modes or $\tilde{u}(1,0) = 1$ for odd modes. Energy growth rates β were computed from

$$\beta = \lim_{t\to\infty} \frac{\ln(\text{energy})}{t} \tag{21}$$

where 'energy' is the sum of the squares of all the mode amplitudes, an L_2 norm definition. It was necessary to integrate for a long time to approach an asymptote in this formula. Over the range computed we have found that the cutoff $M = 40$ was adequate. The results are presented in two figures. Figure 2 shows the neutral curve ($\beta = 0$) for both even and odd modes up to Reynolds numbers of 2000. The band of unstable wavenumbers rapidly expands with increasing Reynolds number. Figure 3 shows the growth rate β versus wavenumber k_z at Reynolds number 2000. Computations at Reynolds numbers 200, 500 and 1000 are similar, with a pronounced notch in the odd-mode curve. The growth rate curves computed by Robinson & Saffman (1984) for the strained vortex have a similar shape made up of the union of separate growth rate curves, for modes with differing internal structure, which look like inverted parabolas. The growth rate at their second peak (multiplying their result by 2 to get energy growth rate) is about 0.3 for $E = 2$, which is comparable to our value of about 0.24.

A result for unstable plane waves in the unbounded flow with elliptical streamlines

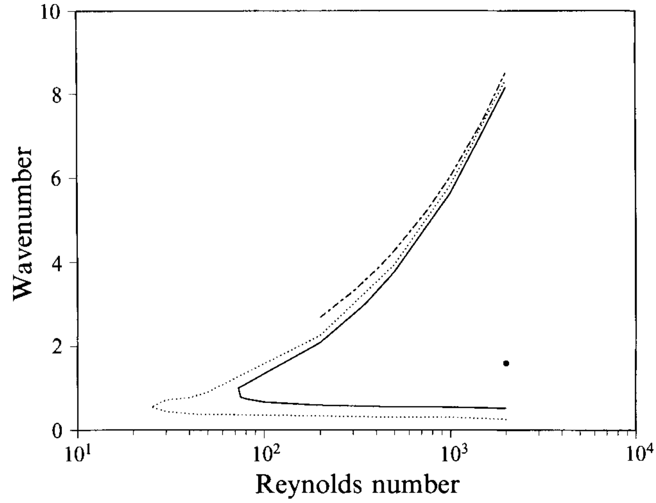

FIGURE 2. Neutral stability curves, $E = 2$: ——, even modes; ·····, odd modes. Heavy dot is at the lowest wavenumber used in the computations. The dot-dash curve is computed from equation (26).

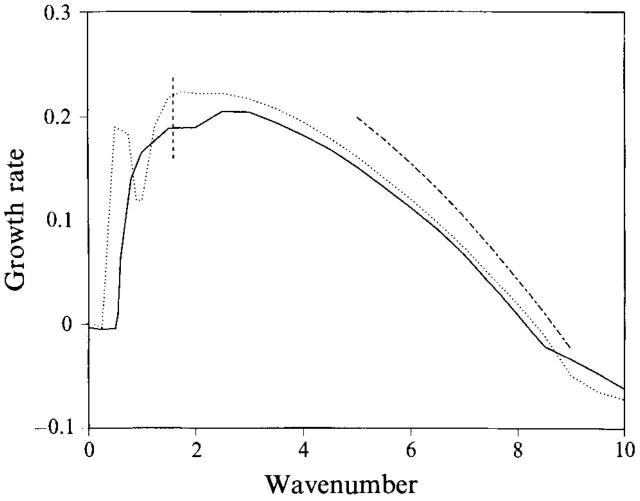

FIGURE 3. Growth rate versus axial wavenumber at $R_e = 2000$, $E = 2$: ——, even modes; ·····, odd modes. The vertical dashed line is at the lowest wavenumber used in the computation. The dot-dash curve is computed from equation (25).

may be obtained from Landman & Saffman (1987):

$$\frac{\beta}{\omega_0} = 2\left(\frac{\sigma_0}{\omega_0} - \nu K^2\right) \tag{22}$$

where ω_0 is the uniform vorticity, σ_0 is the inviscid amplitude growth rate and $K^2 = k_x^2 + k_y^2 + k_z^2$. The factor 2 is inserted to convert to energy growth rate. Now σ_0/ω_0 is a function of ϵ/γ [$= (E^2-1)/(E^2+1)$] where ϵ is strain rate and γ is $\omega_0/2$. For $\epsilon/\gamma < 0.7$ ($E < 2.4$) it is approximately (from a figure in Landman & Saffman)

$$\frac{\sigma_0}{\omega_0} = \frac{1}{2}\left(\frac{9}{16}\left(\frac{\epsilon}{\gamma}\right) - 0.1\left(\frac{\epsilon}{\gamma}\right)^2\right). \tag{23}$$

For an unstable wave with maximum growth rate the wave vector makes an angle of 60° with the rotation axis, therefore $k_x^2 + k_y^2 = 3k_z^2$. Using this and $\nu = 1/R_e$ gives

$$\frac{\beta}{\omega_0} = 2\left(\frac{\sigma_0}{\omega_0} - \frac{4k_z^2}{R_e}\right). \tag{24}$$

For our case with $E = 2$ and $\omega_0 = 1$ we get

$$\beta = 0.3 - \frac{8k_z^2}{R_e}. \tag{25}$$

For fixed R_e this curve is a broad downward facing parabola. A portion of this curve is plotted on figure 3. A neutral curve may be derived from (25), namely

$$k_z = 0.19R_e^{1/2}. \tag{26}$$

This is plotted on figure 2 where the agreement is seen to be quite good at the larger Reynolds numbers. Equations (25) and (26) should allow a reasonable extrapolation to Reynolds numbers larger than those for which we have done computations. At higher Reynolds number the growth rate versus wavenumber curve would become stretched out to a higher zero crossing value while the low-wavenumber end with the bumps would be relatively unchanged because of the small effect of Reynolds number at small wavenumber.

We conclude that the stability results are similar, and have comparable growth rates, to those for bending waves on a concentrated vortex at small wavenumber and are similar to results for an unbounded flow with elliptical streamlines at large wavenumber.

3. Transition to turbulence

Nonlinear computations have been performed on the Intel Hypercube (i860) at NASA-Ames Research Center using two versions of Rogallo's (1981) box code (the 'pencil' codes) written recently by Rogallo for this parallel processing machine. The first version was designed to solve the Navier–Stokes equations in a box with periodic boundary conditions. The box is not required to have equal sides but must be restricted to a volume $(2\pi)^3$. We have taken the sides of the periodic box to be $2L_1 \times 2L_2 \times L_3$ with the x and y dimensions double the size of the impenetrable box. By using proper symmetry in the initial conditions we can ensure that there is no flow across the surfaces $x = 0$ and L_1 and $y = 0$ and L_2. (This is clearly not the most efficient way to solve this problem.) The finite dimension in the z-direction means that L_3 is the longest axial wavelength allowed. Defining $b_1 = \pi/L_1, b_2 = \pi/L_2$ as before and $b_3 = 2\pi/L_3$, the volume constraint makes $b_1b_2b_3 = 1$. Allowed values of the axial wavenumber are therefore $k_z = b_3k$, where k is an integer. Solutions in this periodic system are thus of the form

$$u(x,y,z,t) = \sum_{m,n,k=-N/2}^{N/2-1} \tilde{u}(m,n,k) \exp \mathrm{i}(mb_1x + nb_2y + kb_3z) \tag{27}$$

with similar expressions for $v(x,y,z,t)$ and $w(x,y,z,t)$.

Conjugate symmetry ($\tilde{u}(-m,-n,-k) = \tilde{u}(m,n,k)^*$, etc.) is imposed to ensure that the velocity components are real. Symmetries in the initial conditions are taken

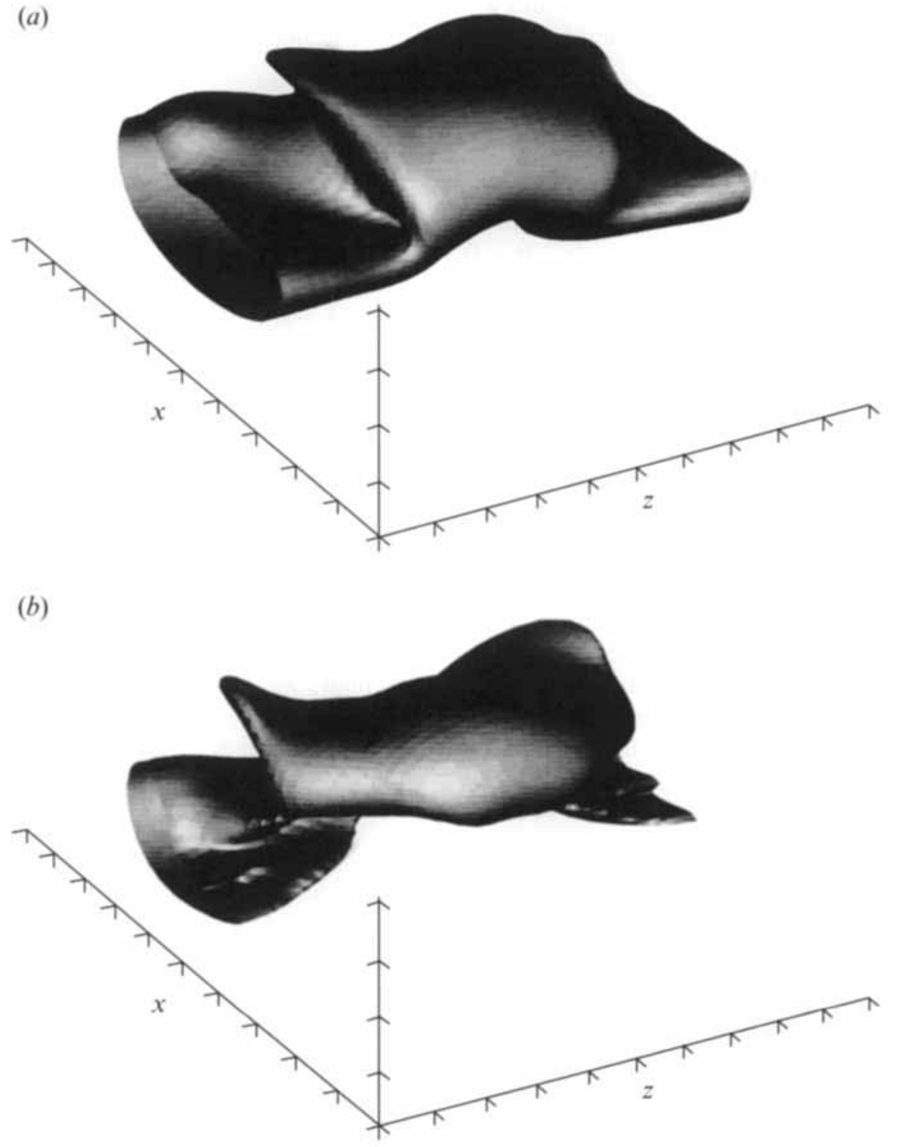

FIGURE 4(*a*, *b*). For caption see page 52.

like those in (15)–(20) for each k. For instance the velocity field of the basic flow, $U = b_2 \sin b_1 x \cos b_2 y/(b_1^2 + b_2^2)$, $V = -b_1 \cos b_1 x \sin b_2 y/(b_1^2 + b_2^2)$ is generated by the four modes

$$\tilde{u}(1,1,0) = \tilde{u}(1,-1,0) = -\tilde{u}(-1,1,0) = -\tilde{u}(-1,-1,0) = -\frac{b_2 \mathrm{i}}{4(b_1^2 + b_2^2)}, \qquad (28a)$$

$$\tilde{v}(1,1,0) = -\tilde{v}(1,-1,0) = -\tilde{v}(-1,1,0) = \tilde{v}(-1,-1,0) = -\frac{b_2 \mathrm{i}}{4(b_2^2 + b_2^2)}, \qquad (28b)$$

which have these symmetries. Perturbations from this basic flow can be generated in many different ways and will generate different flows. For instance we could have

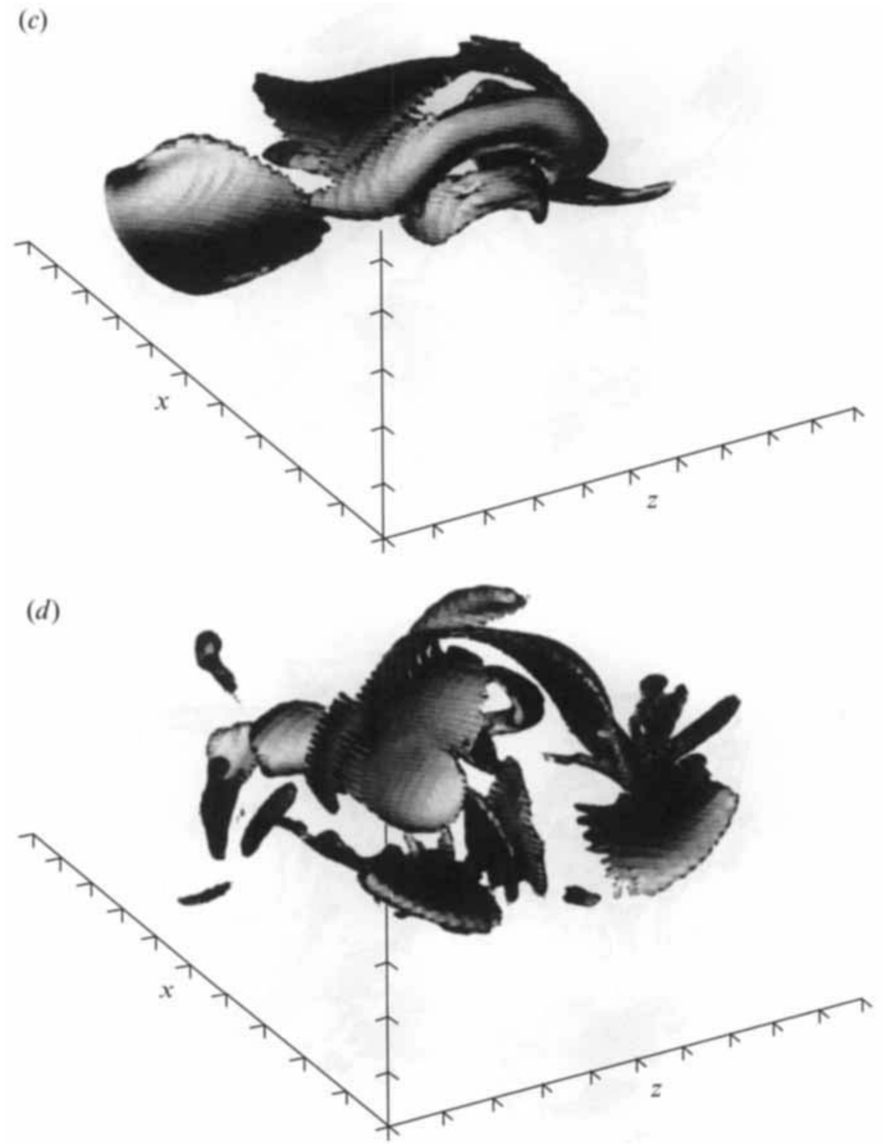

FIGURE 4(*c*, *d*). For caption see page 52.

used random small initial perturbations. For the flow computed here, however, we excited both even and odd modes uniformly by

$$u' = \sum_k (0.001 \sin b_1 x \cos b_3 kz + 0.001 \sin 2b_1 x \cos b_3 kz) \tag{29}$$

with $v' = 0$ and the corresponding w' determined from continuity. The initial mode amplitudes are therefore

$$\tilde{u}(1,0,k) = -\tilde{u}(-1,0,k) = \tilde{u}(1,0,-k) = -\tilde{u}(-1,0,-k) = -0.001\mathrm{i}/4, \tag{30a}$$

$$\tilde{u}(2,0,k) = -\tilde{u}(-2,0,k) = \tilde{u}(2,0,-k) = -\tilde{u}(-2,0,-k) = -0.001\mathrm{i}/4 \tag{30b}$$

for all integer k in wave space. (Although all wavenumbers were excited only the

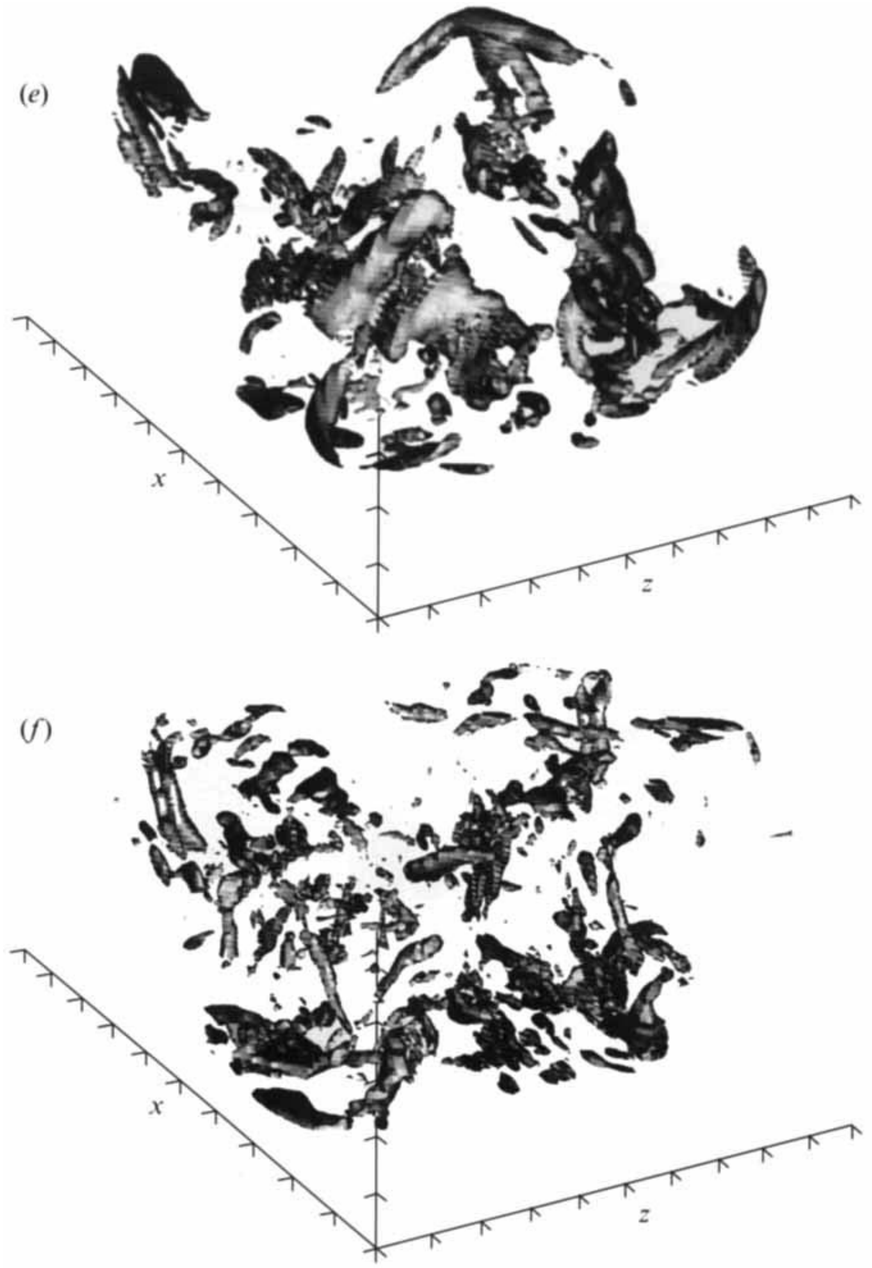

FIGURE 4. Surfaces of vorticity, $R_e = 2000$. Tick marks are at 0.6 intervals in the x-direction and at 0.4 intervals in the y- and z-directions. (*a*) Vorticity equal to 0.75 at $T = 55.66$. The maximum vorticity is 2.01. (*b*) Vorticity 1.04 at $T = 61.71$, maximum vorticity 2.78. (*c*) Vorticity 2.06 at $T = 70.43$, maximum vorticity 5.50. (*d*) Vorticity 3.60 at $T = 79.09$, maximum vorticity 9.61. (*e*) Vorticity 4.95 at $T = 83.94$, maximum vorticity 13.19. (*f*) Vorticity 5.89 at $T = 87.95$, maximum vorticity 15.70.

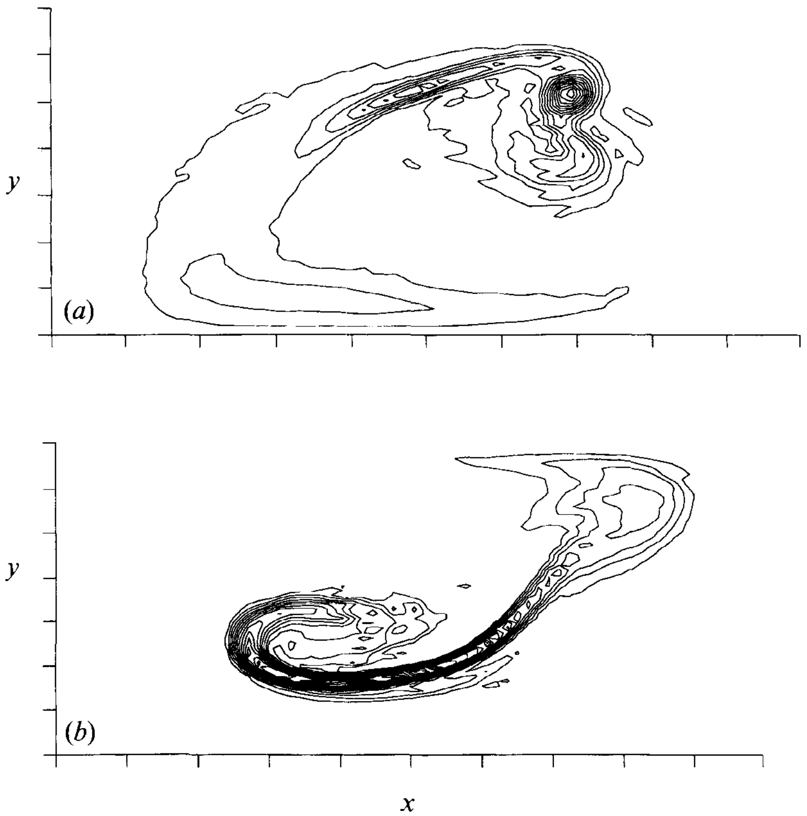

FIGURE 5. Vorticity contours at the time corresponding to figure 4(*c*); (*a*) on the plane $z = 0.5L_3$; (*b*) on the plane $z = 0$. $R_e = 2000$. View is along the z-axis. Intervals on the axes are the same as on figure 1.

lowest few matter because of the rapid decrease of growth rate with increasing wavenumber.) With the cosine dependence in the z-direction in (29) the endwalls and the midplane $z = L_3/2$ will also be impenetrable ($w = 0$).

Finally we chose to do the computation with $E = 2 = L_1/L_2$ and $L_3 = (L_1L_2)^{1/2}$. The volume constraint then makes $L_1 = 5.60, L_2 = 2.8, L_3 = 3.96$ and then $b_1 = 0.56, b_2 = 1.12$ and $b_3 = 1.59$. We have computed with $R_e = 2000$ and $N = 128$. (Another form of Reynolds number which could be useful is $\Gamma/\nu = 12\,755$ where Γ is the circulation of the basic flow around the impenetrable box.) The lowest wavenumber in the initial conditions, $k_z = 1.59$, is shown in the stability diagrams as a heavy dot in figure 2 and as a vertical dashed line in figure 3. It is near the position of maximum growth rate: the dimensions of the box were chosen for this reason. With $N = 128$, the actual resolution in the impenetrable box is $64 \times 64 \times 128$.

A second version of Rogallo's code is more efficient for this computation and was run at a higher Reynolds number. In this version sine and cosine FFT's were implemented to maintain impenetrability of the sidewalls so that the computation could be confined to the impenetrable box alone. We have run this with 256^3 resolution at $R_e = 5000$ ($\Gamma/\nu = 31\,888$) with the same box dimensions and initial conditions described above.

The major results of the computations at $R_e = 2000$ are presented in figure 4 (a–f),

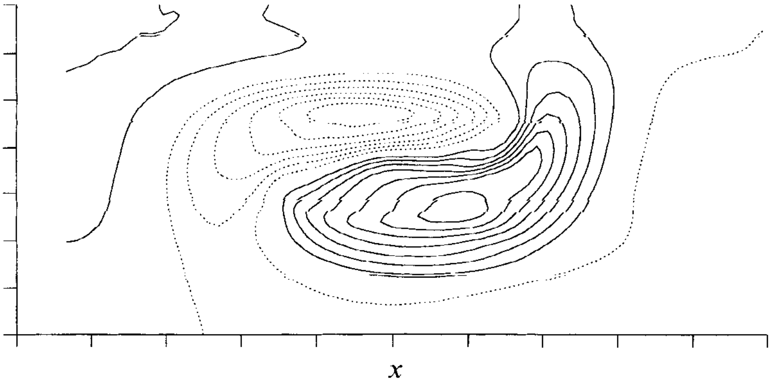

FIGURE 6. Contours of axial velocity on the plane $z = 0.25L_3$ at the time corresponding to figure 4(*c*). $R_e = 2000$. View is along the *z*-axis. Solid contours are for velocity into the page, dotted contours are out of page. Maximum velocities are ± 0.35. Intervals on the axes are the same as on figure 1.

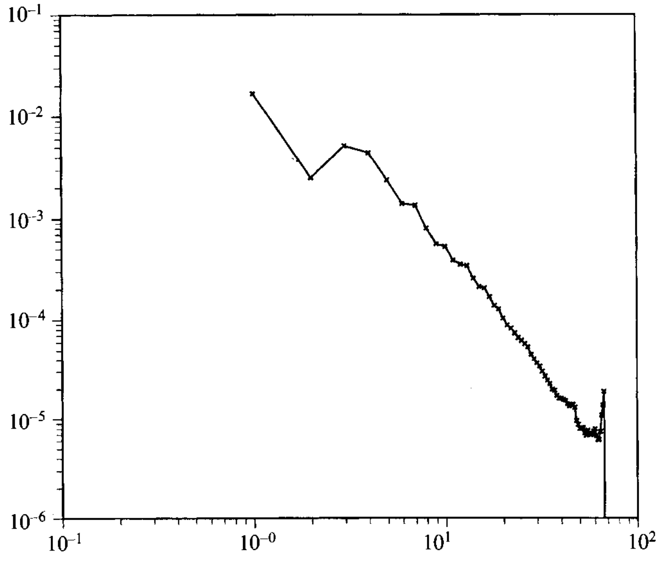

FIGURE 7. Spectral density versus wavenumber at $T = 87.95$. $R_e = 2000$. A line connecting the corners of the box would be $k^{-5/3}$.

where surfaces of constant magnitude of the vorticity are shown at six different times during the evolution of this flow. In each part of the figure the surface is of the vorticity value that is 3/8 of the maximum vorticity at this time. The time and the values of the surface vorticity and maximum vorticity are given in the figure caption. The coordinate axes shown have *x* to the left, *y* vertical and *z* off to the right. The viewpoint and illumination are from the origin. At the initial time (not shown) the surface is approximately an elliptic cylinder. The instability causes distortion into a wave oriented roughly along a 45° plane with the vortex moving downward and toward positive *x* at the ends of the box and upward and toward negative *x* in the middle. The secondary flow which causes this motion also causes the vortex to be greatly distorted into sheet-like structures which resemble the 'cups' found by Rogers & Moser (1992) in their study of the development of three-dimensional structure in a

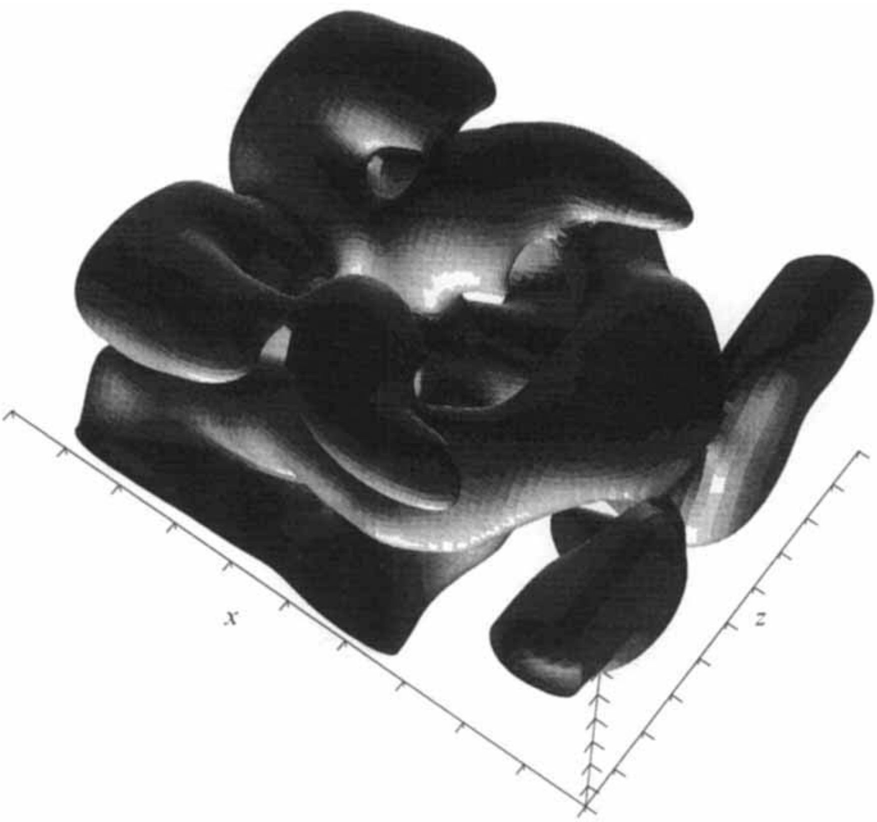

FIGURE 8. Surface of Gaussian filtered vorticity equal to 0.45 at $T = 87.95$. The maximum filtered vorticity is 1.19. $R_e = 2000$. Tick marks are the same as on figure 4.

mixing layer after the primary rollup into spanwise rollers. In figures 5(*a*) and 5(*b*) we look at vorticity contours on cuts through the structure shown in figure 4(*c*) in order to elucidate its structure. In figure 5(*a*) we have taken the cut through the middle of the structure along the plane $z = L_3/2$, with the view along the z-axis (positive z is into the page). Because of the symmetry imposed in the initial conditions only the z-component of vorticity is nonzero on this plane. The maximum vorticity in the box, 5.5, occurs at the centre of the rather strong round vortex which is apparent here. In the three-dimensional rendering this vortex appears to be like a horseshoe vortex. In figure 5(*b*) the cut is at the ends of the box at plane $z = 0$, where again only ω_z is non-zero and the view is along the z-axis. The maximum vorticity in the strong vortex layer is 3.5.

In figure 6 we show contours of the axial velocity w in the plane $z = 0.25L_3$ through the structure shown in figure 4(*c*). This is more regular than might have been expected and shows characteristics of the 1,1 mode in Robinson & Saffman (1984). (The first 1 refers to the angular wavenumber and the second to the number of nodes in the axial velocity.) Here despite the already complicated vorticity the underlying secondary flow of the instability is still evident, much amplified, with maximum velocities ± 0.35. Since w is zero at both ends of the box and in the middle, and w on the plane $z = 0.75L_3$ is just the reverse of that shown in figure 6, we can picture the secondary flow as two eddies, one in each half of the box, with the velocity toward the centre

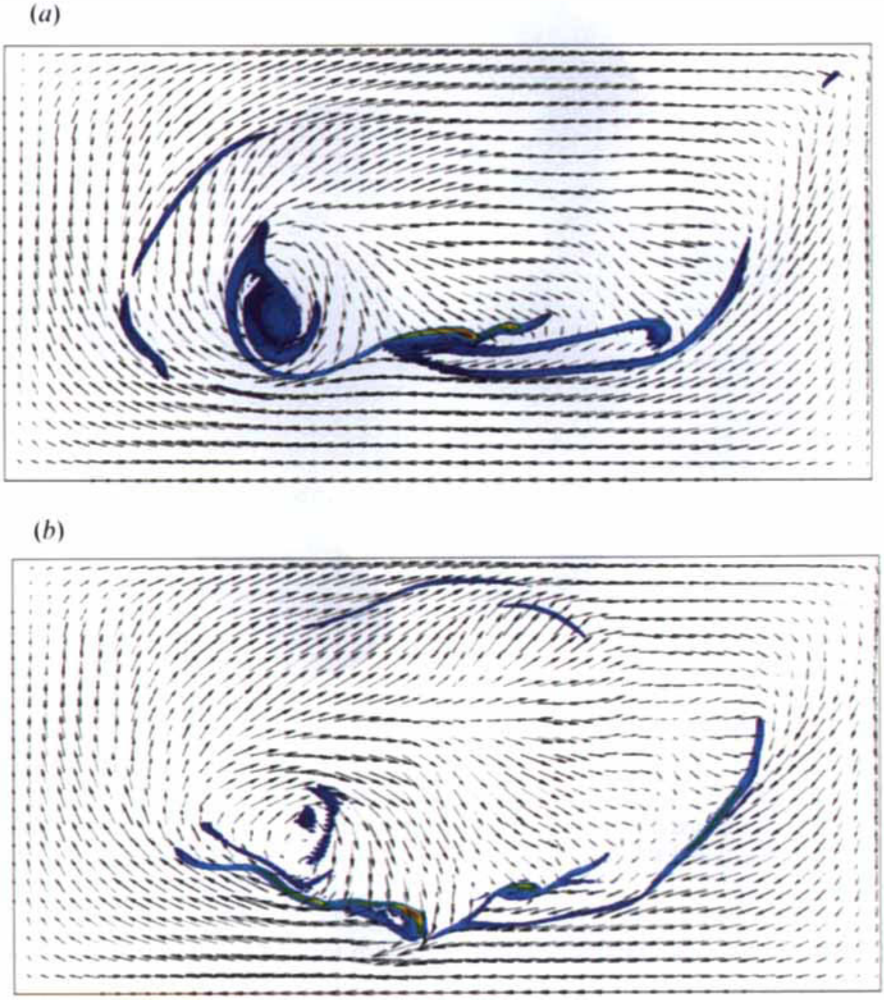

FIGURE 9(a,b). For caption see facing page.

of the box in the lower part and away from the centre above. Completion of this circulation is such as to convect the vorticity downwards and toward positive x at the ends while stretching it, and convecting it upward and toward negative x in the middle, stretching it here also. It is remarkable that this secondary motion is evident throughout the entire sequence of views, even at the time of figure 4(f) where it is quite irregular but with the main trends described above.

As we proceed from figure 4(c) to figure 4(d) the strong vortex which was evident in figure 4(c) has disappeared. The central part has apparently been carried downward into the compressive part of the circulation which decreased its vorticity below the plotting level. The remnants of its sides have been stretched into the shield-shaped vortex sheets to each side of the centre. In the next view, figure 4(e), there is no vorticity at the level plotted, across the plane $z = 0.5L_3$. This is not clear from the figure but when we rotated it we had an open view down the middle. The structures we see are mostly tube-like now, and this is even more evident in figure 4(f), which is the time at which the maximum vorticity in the box is largest. At later times this

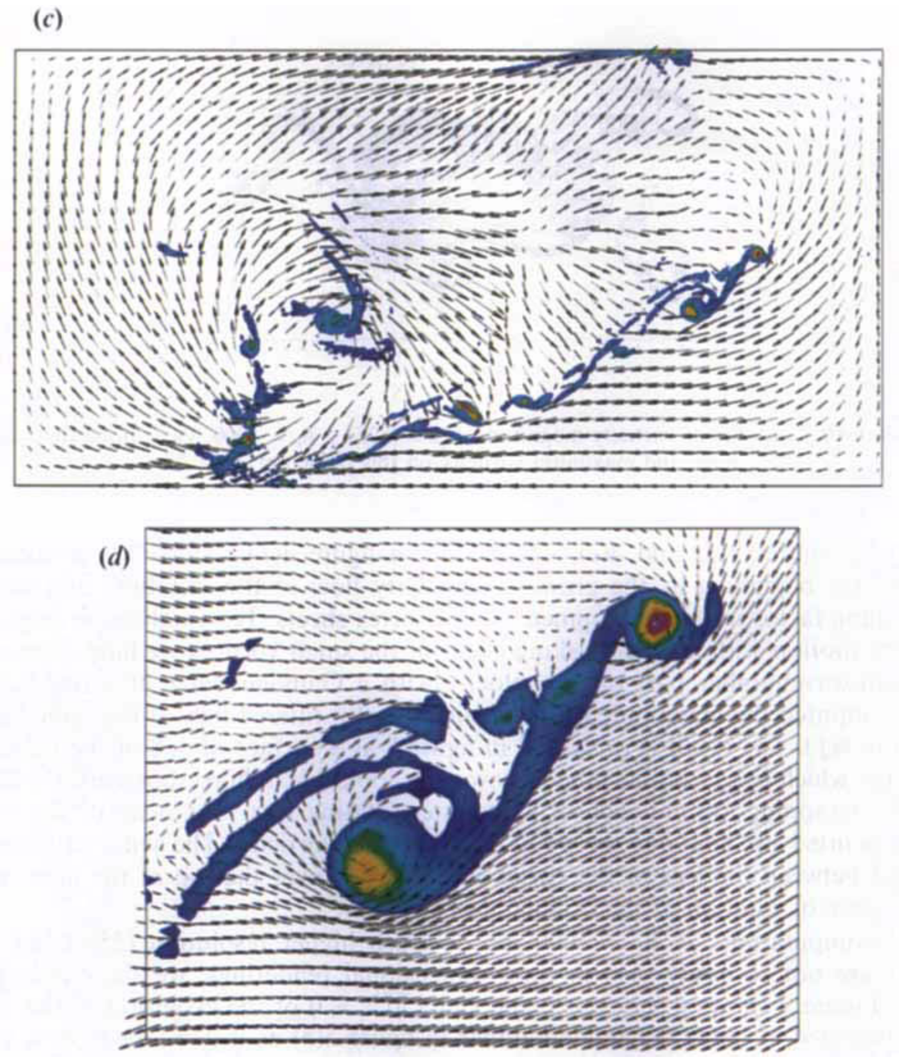

FIGURE 9. Vorticity contours at $z = 0$ at selected times showing evolution of the vortex layer into vortex tubes. View is along the z-axis. $R_e = 5000$. Time and maximum vorticity in the plane are: (*a*) 66.8, 19; (*b*) 69.7, 26; (*c*) 72.0, 34; (*d*) is an enlarged view of the right-hand side of (*c*). Colours range from blue at a vorticity of 3 to red at the maximum vorticity. Velocity vectors in (*a*, *b*, *c*) are plotted with a scale factor of 0.4 with 5.8 units of length along the horizontal boundary. In (*d*) the scale factor is 0.1 with 1.02 units of length along the horizontal. (To convert to velocity one divides the vector length by the scale factor.)

begins to decrease but the tube-like nature of the vorticity is still evident at the time of 103.8 when we ended the computation.

Figure 7 shows the average of the three velocity component power spectra at the time of figure 4(*f*). (The energy spectrum is 1.5 times this quantity.) While this is quite broad, indicating turbulence, we do not see a $-5/3$ range at this Reynolds number. (In fact it is close to a $-7/3$ power.) At the higher Reynolds number we do find a $-5/3$ range.

The overall impression of this flow is of two large counter-rotating turbulent eddies, each carrying many intense interacting vortex tubes. One can see their development

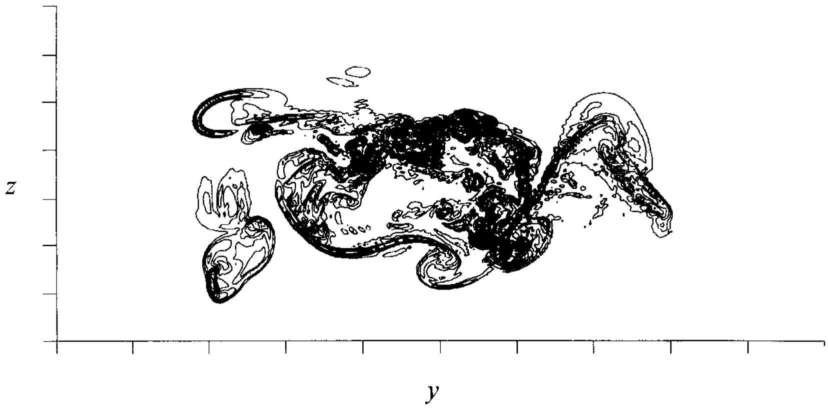

FIGURE 10. Contours of vorticity magnitude at $z = 0.25L_3$. $R_e = 5000$. View along the z-axis. Time and maximum vorticity on this plane are: 69.7, 22.

clearly in figures 4(*d*) and 4(*e*), less clearly in figure 4(*f*). This eddy motion was present the beginning as the growing secondary flow of the instabilty and was the controlling factor in the development of the vortex sheets. To visualize the large-scale swirling motion without the masking effect of the small vortices we have filtered out the high-wavenumber part of the velocity with a Gaussian filter of width 0.2. We have computed the magnitude of the vorticity in this filtered flow at the same time as in figure 4(*f*). The result is presented in figure 8 as a surface of 3/8 of the maximum vorticity, which is 1.19 in this filtered flow. This looks like a horseshoe vortex with two vortices wrapping around each of its counter-rotating legs. The head of the vortex, which is lifted up, contains the point of maximum vorticity. The sense of motion is upward between the legs of the vortex and forward over the top of the nose, which is the sense of rotation of the original swirling flow

The computations at $R_e = 5000$ are of much higher resolution (256^3) but since details are not so easily seen in three-dimensional renderings, we show only plane views. Figure 9 shows a series of plane views at $z = 0$ of the evolution of the vortex sheet depicted at lower Reynolds number in figure 5(*b*) as it develops from a vortex sheet to a number of vortex tubes. (The times shown on the figure are earlier than on figure 5(*b*) because the vortex sheet develops faster at this higher Reynolds number.) The vortices appear to develop by the Kelvin–Helmholtz instability or by a version of this instability which involves stretching a vortex layer along the direction of the vorticity while simultaneously compressing it. This process has been studied by Lin & Corcos (1984) and by Neu (1984). Passot *et al.* (1994) have suggested that this mechanism is the origin of the vortex tubes observed in numerical simulations of homogeneous turbulence. Stretching is clearly involved in the present flow since the maximum vorticity on the plane grows from about 3.5 in figure 5(*b*) to about 34 in figure 9(*c*): this can only be caused by vortex stretching since the vorticity has only a z-component on this plane and the z-component of the velocity is zero. Besides non-uniform stretching there is a general clockwise circulation on this plane. In figure 9(*a*), which is at a later stage of development than in figure 5(*b*) the structure of the vorticity is still quite sheet-like but with several regions of more intense vorticity. In figure 9(*b*) the intense regions have become further concentrated and stronger. On the vortex layer which is to the left of the red spot there is a waviness which looks like a secondary instability. Moser & Rogers (1993) show a similar secondary

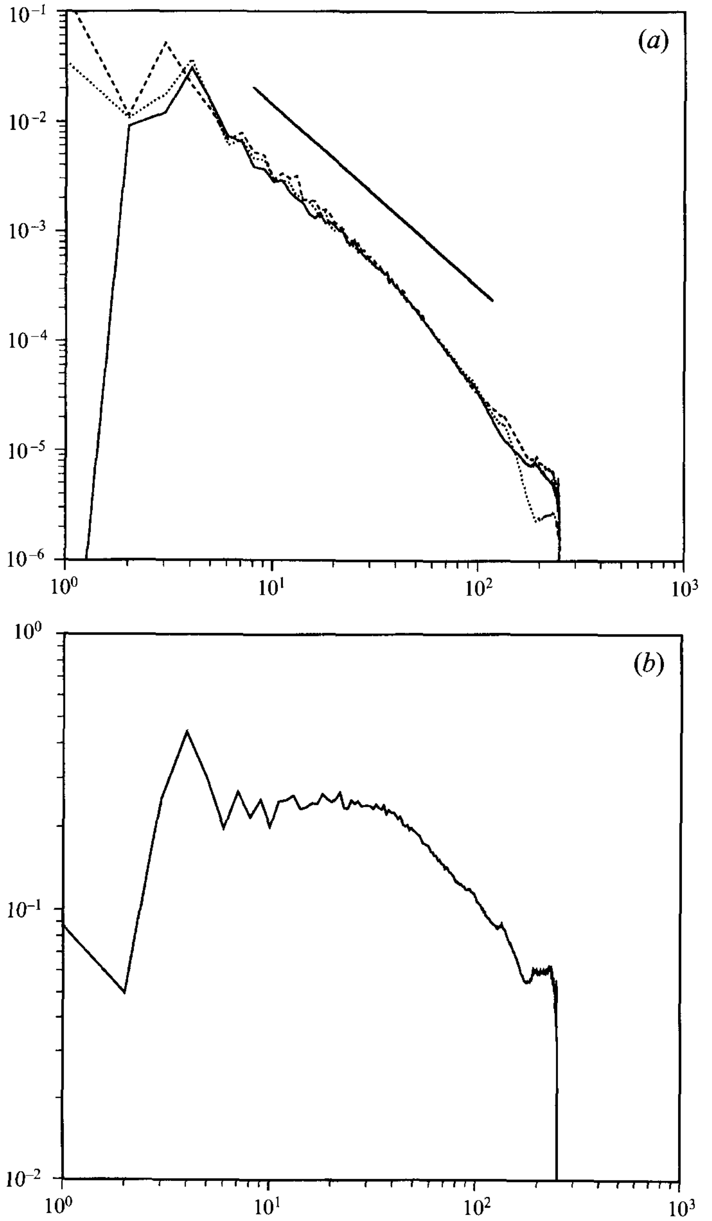

FIGURE 11. (*a*) Three-dimensional power spectra of the component velocities versus wavenumber: — — — — —, u^2 spectrum; · · · · · ·, v^2 spectrum; ———, w^2 spectrum. The straight line on the figure is $k^{-5/3}$. (*b*) Energy spectrum times $k^{5/3}$.

instability on stretching vortex sheets which appeared during the pairing process in a plane mixing layer computation. Figure 9(*c*) shows a number of strong vortices with weaker thin vortex layers spiralling around them. A portion of the right-hand side of this figure which shows this feature particularly well has been enlarged as figure 9(*d*). Spiral structures were observed by Passot *et al.* (1994) in a homogeneous turbulence computation.

The contour plots in figure 9 are not completely typical of this flow because of the symmetry of the flow at this plane. In figure 10 we show a single contour plot of the magnitude of the vorticity on the plane $z = 0.25L_3$ at the time $T = 69.7$. This shows many of the same features as figure 9. However, these vortices are not perpendicular to the plane and have vorticity of both signs. In fact the vorticity on this plane is nearly isotropic with the x-component ranging from -15 to $+21$, the y-component from -14 to $+12$ and the z-component from -19 to $+16$.

Three-dimensional velocity power spectra of the individual velocity components have been computed by shell averaging in wavenumber space. Figure 11(*a*) shows the three component spectra at a time $T = 79.8$ from the $R_e = 5000$ computation and figure 11(*b*) is a plot of the energy spectrum times $k^{5/3}$. The figures show that the component spectra are nearly the same except at the lowest wavenumbers. This is a necessary condition for isotropy. They also show somewhat less than a decade of the $k^{-5/3}$ power law, approximately from $k = 6$ to $k = 35$. Small-scale isotropy was already pronounced at time $T = 72$ but with a shorter Kolmogorov range. The existence of local isotropy in turbulent shear flows has long been controversial. Saddoughi & Veeravalli (1994) give a brief history of the issues and present new measurements which show isotropy in the inertial and dissipation spectral ranges in a large wind tunnel boundary layer.

4. Discussion and conclusions

We have studied the stability and transition to turbulence in a confined elliptic vortex. This relatively simple nonuniform shear flow is similar to embedded elliptic structures found in many naturally occurring flows. As the turbulence develops it consists of a large number of interacting vortex tubes which remain some distance from the cell boundaries in a large turbulent structure which resembles the horseshoe vortices found in turbulent boundary layers. Because of the simple geometry of this flow and its close connection with real flows an important application of this flow should be as a test case for large-eddy simulation (LES) models.

Transition to turbulence in this flow is by very simple mechanisms, which may prove to be typical. The elliptic instability compresses the primary vorticity into thin vortex layers and these develop a second instability which forms into elongated vortex tubes. After the vortex tubes appear the flow is fully turbulent as can be recognized by the broad energy spectrum.

The conventional picture of turbulence is due to Richardson (1922). The interpretation of his ideas, presented by Monin & Yaglom (1971), is that turbulence consists of a hierarchy of eddies of various orders. Eddies of a given order arise as a result of the *loss of stability* of larger eddies of the previous order, borrowing their energy, and these in turn lose their stability and transfer their energy to even smaller eddies. Thus there is a cascade of energy from large eddies to small. There has always been controversy over the nature of 'eddies' and some researchers prefer to think in terms of Fourier components, replacing 'eddy' by 'wavelength' in the above description. Our observations involve only two instabilities, instead of the continuum of instabilities which would seem to be required, and it is clear that much of the energy cascade takes place by continuous deformation after the vortex tubes appear. Vincent & Meneguzzi (1994) suggest that the energy cascade is a one-step process involving the rollup of vortex sheets. Lundgren (1982) and Pullin & Saffman (1992) have developed a turbulence model which has a continuous energy cascade. We describe this model briefly here because of its similarity to the flow in the present computation. The model consists of an ensemble of randomly oriented spiral vortex solutions of the

Navier–Stokes equations. In the inviscid limit these solutions consist of spiral vortex sheets in which the inner turns continually tighten by differential rotation while the vortex is being stretched along its axis (by larger scale motions). Both of these mechanisms cause a cascade of energy to smaller scales. With finite viscosity the inner turns are diffused together into a smooth vortex core and for moderate Reynolds numbers these vortices are similar to those found in the present computations, with partial spirals around central cores. The model gives a rational derivation of the $k^{-5/3}$ Kolmogorov energy spectrum and thus connects this spectrum with spiral vortices, which are observed in the present computation. It should be pointed out that spiral vortices are commonly seen in experimental turbulent flow visualizations, but are more difficult to find in computations.

The authors would like to acknowledge several very useful discussions with Dr Karim Shariff and we would like to thank him and Dr Javier Jimenez for reviewing this manuscript. We are especially grateful to Dr Robert Rogallo of NASA-Ames for allowing us to use his computer program. T.S.L. was partially supported by NASA-Ames Research Center (1994) and by the Center for Turbulent Research at NASA-Ames/Stanford University (1993). While the bulk of the computations were done at NASA-Ames at the NAS computational facility, we would also like to acknowledge a computer grant from the Minnesota Supercomputer Institute.

REFERENCES

Bayly, B. J. 1986 Three-dimensional instability of elliptical flow. *Phys. Rev. Lett.* **57**, 2160–2163.

Bayly, B. J. 1989 Computations of broad-band instabilities in a class of closed-streamline flows. In *Mathematical Aspects of Vortex Dynamics* (ed. R. E. Caflisch), pp. 50–58. SIAM.

Bayly, B. J., Orszag, S. A. & Herbert, T. 1988 Instability mechanisms in shear-flow transition. *Ann. Rev. Fluid Mech.* **20**, 359–391.

Gledzer, Ye. B., Dolzhanskiy, F. V., Obukhov, A. M. & Ponomarev, V. M. 1975 An experimenal and theoretical study of the stability of motion of a liquid in an elliptic cylinder. *Izv. Atmos. Ocean. Phys.* **11**, 981–992.

Gledzer, Ye. B., Novikov, Yu. V., Obukhov, A. M. & Chusov, A. M. 1974 An investigation of the stability of liquid flows in a three-axis ellipsoid. *Izv. Atmos. Ocean. Phys.* **10**, 115–118.

Jimenez, J., Wray, A. A., Saffman, P. G. & Rogallo, R. S. 1993 The structure of intense vorticity in isotropic turbulence. *J. Fluid Mech.* **255**, 65–90.

Kerr, R. M. 1985 Higher-order derivative correlations and the alignment of small-scale structures in isotropic numerical turbulence. *J. Fluid Mech.* **153**, 31–58.

Landman, M. J. & Saffman, P. G. 1987 The three-dimensional instability of strained vortices in a viscous fluid. *Phys. Fluids* **30**, 2339–2342.

Lin, S. J. & Corcos, G. M. 1984 The mixing layer: deterministic models of a turbulent flow. Part 3. The effect of plane strain on the dynamics of streamwise vortices. *J. Fluid Mech.* **141**, 139-178.

Lundgren, T. S. 1982 Strained spiral vortex model for turbulent fine structure. *Phys. Fluids* **25**, 2193–2203.

Malkus, W. V. R. 1989 An experimental study of global instabilities due to the tidal (elliptical) distortion of a rotating elastic cylinder. *Geophys. Astrophys. Fluid Dyn.* **48**, 123–134.

Monin, A. S. & Yaglom, A. M. 1971 *Statistical Fluid Mechanics*, Vol. 1. MIT Press.

Moore, D. W. & Saffman, P. G. 1975 The instability of a straight vortex filament in a strain field. *Proc. R. Soc. Lond.* A **346**, 413–425.

Moser, R. D. & Rogers, M. M. 1993 The three-dimensional evolution of a plane mixing layer: pairing and transition to turbulence. *J. Fluid Mech.* **247**, 275–320.

Neu, J. C. 1984 The dynamics of stretched vortices. *J. Fluid Mech.* **143**, 253–276.

Orszag, S. A. & Patera, A. T. 1983 Secondary instability of wall-bounded shear flows. *J. Fluid Mech.* **128**, 347–385.

PASSOT, T., POLITANO, H., SULEM, P. L., ANGILELLA, J. R. & MENEGUZZI, M. 1994 Instability of strained vortex layers and vortex tube formation in homogeneous turbulence. *J. Fluid Mech.* **282**, 313–338.

PIERREHUMBERT, R. T. 1986 Universal short-wave instability of two dimensional eddies in an inviscid fluid. *Phys. Rev. Lett.* **57**, 2157–2159.

PULLIN, D. I. & SAFFMAN, P. G. 1992 On the Lundgren-Townsend model of turbulent fine scales. *Phys. Fluids* A **5**, 126–145.

RICHARDSON, L. F. 1922 *Weather Prediction by Numerical Process*. Cambridge University Press.

ROBINSON, A. C. & SAFFMAN, P. G. 1984 Three-dimensional stability of an elliptical vortex in a straining field. *J. Fluid Mech.* **142**, 451–466.

ROGALLO, R. S. 1981 Numerical experiments in homogeneous turbulence. *NASA Tech. Mem.* 81315.

ROGERS, M. M. & MOSER, R. D. 1992 The three-dimensional evolution of a plane mixing layer: the Kelvin–Helmholtz rollup. *J. Fluid Mech.* **243**, 183–226.

SADDOUGHI, S. G. & VEERAVALLI, S. V. 1994 Local isotropy in turbulent boundary layers at high Reynolds number. *J. Fluid Mech.* **268**, 333–372.

SHE, Z. S., JACKSON, E. & ORSZAG, S. A. 1990 Structure and dynamics of homogeneous turbulence, models and simulations. *Proc. R. Soc. Lond.* A **434**, 101–124.

VINCENT, A. & MENEGUZZI, M. 1991 The spatial structure and statistical properties of homogeneous turbulence. *J. Fluid Mech.* **225**, 1–20.

VINCENT, A. & MENEGUZZI, M. 1994 The dynamics of vorticity tubes in homogeneous turbulence. *J. Fluid Mech.* **258**, 245–254.

WALEFFE, F. 1989 The 3D instability of a strained vortex and its relation to turbulence. PhD Thesis, Massachusetts Institute of Technology.

WALEFFE, F. 1990 On the three-dimensional instability of strained vortices. *Phys. Fluids* A **2**, 76–80.

WIDNALL, S. E., BLISS, D. B. & TSAI, C.-Y. 1974 The instability of short waves on a vortex ring. *J. Fluid Mech.* **66**, 35–47.